



# Transforming type-I to type-II heterostructure photocatalyst via energy band engineering: A case study of I-BiOCl/I-BiOBr

Xuemei Jia <sup>a</sup>, Jing Cao <sup>a,b</sup>, Haili Lin <sup>a,b,c,\*</sup>, Meiyu Zhang <sup>a</sup>, Xiaomin Guo <sup>a</sup>, Shifu Chen <sup>a,\*\*</sup>

<sup>a</sup> College of Chemistry and Materials Science/Information College, Huaibei Normal University, Huaibei 235000, Anhui, PR China

<sup>b</sup> Anhui Key Laboratory of Energetic Materials, Huaibei, 235000 Anhui, PR China

<sup>c</sup> State Key Laboratory of Structural Chemistry, Fuzhou, 350002 Fujian, PR China



## ARTICLE INFO

### Article history:

Received 28 September 2016

Received in revised form

17 November 2016

Accepted 29 November 2016

Available online 29 November 2016

### Keywords:

I-BiOCl/I-BiOBr

Heterojunction

Doping effect

Energy band engineering

## ABSTRACT

Double visible light driven type-II heterostructure composites display highly efficient separation efficiency of photocharges due to the matching energy band structure. On the basis of the energy band engineering strategy, a novel flower-like heterostructured I-BiOCl/I-BiOBr composite was designed and synthesized by a simple deposition-precipitation method. The as-prepared I-BiOCl/I-BiOBr composites exhibited outstanding photocatalytic properties toward degradation of organic pollutants under visible light irradiation ( $\lambda > 400$  nm). Comparatively, 20% I-BiOCl/I-BiOBr showed the highest photocatalytic activity owing to the best separation efficiency of photocharges. Based on the Mott-Schottky analysis, the I-BiOCl and I-BiOBr formed new  $I^-$  ion doping energy level located on top of the valence bands of BiOCl and BiOBr, respectively. The doping effects presented two advantages: (1) making I-BiOCl and I-BiOBr possess favorable visible light absorption and (2) transforming type-I BiOCl/BiOBr structure to typical type-II I-BiOCl/I-BiOBr system. The strong visible light absorption of I-BiOCl and I-BiOBr as well as the I-BiOCl/I-BiOBr heterojunction interface with highly efficient separation of photocharges resulted in largely enhanced photocatalytic activity of I-BiOCl/I-BiOBr composite system. This study reveals that energy band structure modulation induced by ion doping can overcome the shortcoming of single-component photocatalyst, and play significant role for assembling double visible light driven type-II heterostructure composites.

© 2016 Elsevier B.V. All rights reserved.

## 1. Introduction

Semiconductor photocatalysis has been extensively applied for decomposing organic pollutants [1–3], splitting water to  $H_2$  [4–6], and converting  $CO_2$  into value-added and renewable fuels [7–9]. Due to the weak spatial separation efficiency of photocharges for single-component semiconductor photocatalysts, constructing composite photocatalysts has been considered as useful means to overcome the above-mentioned disadvantage [10,11]. Comparatively, type-II semiconductor heterostructure with matching energy band structures exhibited the best electron-hole separation efficiency [12–16], which guides us to elaborately select suit-

able components for assembling them in a unit composite system [14,16].

Although various type-II semiconductor heterostructures have been successfully designed depending on the intrinsic energy band structure of pure components, a great deal of semiconductor heterostructures still had mismatching type-I and type-III styles [17–19]. This leads to the weak separation efficiency of photocharges in photocatalysis process. Therefore, it is very important to transform the invalid type-I and type-III to highly efficient type-II structure in view of the sufficient utilization of the existing semiconductors. However, it is still a blank area to realize this goal. Considering the effect of ion doping on the energy band structure of photocatalysts, it provides a potential strategy to reform the energy band structures of type-I and type-III heterostructures.

$BiOX$  ( $X = Cl, Br$  and  $I$ ) [20–22] is a novel family of plate-like photocatalysts widely used in organic contaminants degradation. Various  $BiOX$ -based composites [23–27] were developed to enhance the activity of single-component  $BiOX$ . Affected by energy band structure of  $BiOX$ , the self-constructed  $BiOCl/BiOBr$  [28],  $BiOCl/BiOI$  [29] and  $BiOBr/BiOI$  [30] heterostructures had the

\* Corresponding author at: College of Chemistry and Materials Science/Information College, Huaibei Normal University, Huaibei, 235000 Anhui, PR China.

\*\* Corresponding author.

E-mail addresses: [linhaili@mail.ipp.ac.cn](mailto:linhaili@mail.ipp.ac.cn) (H. Lin), [\(S. Chen\).](mailto:chshifu@chnu.edu.cn)

typical type-I energy structure. Therefore, it is a very appropriate model sample to perform the energy band modulation for constructing highly efficient type-II composite.

In this paper, we selected BiOCl/BiOBr as a model to achieve the energy band structure transformation from type-I to type-II. I<sup>−</sup> ions were applied as dopants [31–40] to raise the valence band positions of BiOCl and BiOBr, respectively. Through controlling the doping amount of I<sup>−</sup> ions, the valence band position of I-BiOCl successfully located above that of I-BiOBr. The reformed type-II I-BiOCl/I-BiOBr composite exhibited outstanding photocatalytic activity for methyl orange and phenol degradation under visible light ( $\lambda > 400$  nm). The highly efficient separation of photocharges was ensured by transient photocurrent and surface photovoltage data. We provide a facile way to design novel type-II composites with excellent separation efficiency of photocharges by optimizing type-I composites using dramatic ions doping effect on the energy band structure.

## 2. Experimental

### 2.1. Sample preparation

I-BiOCl was prepared by a chemical precipitation method. 10 mmol Bi(NO<sub>3</sub>)<sub>3</sub>·5H<sub>2</sub>O was first dissolved in a mixed solution containing 15 mL glacial acetic acid and 29 mL deionized water. Then, a 50 mL mixed aqueous solution with NaCl and KI (molar ratio was set as 7:1) was added dropwise into the above-mentioned Bi(NO<sub>3</sub>)<sub>3</sub> solution. After successive stirring for 3 h, the yellow precipitate was collected, washed with deionized water for several times and dried at 80 °C for 12 h in air. Similarly, I-BiOBr sample was also synthesized except that the molar ratio of NaBr to KI was set as 19:1.

I-BiOCl/I-BiOBr sample was fabricated by a simple deposition-precipitation method. Firstly, the as-prepared I-BiOBr was homogeneously dispersed in 50 mL deionized water. After 2 mmol Bi(NO<sub>3</sub>)<sub>3</sub> aqueous solution was added into the above I-BiOBr suspension under vigorous stirring, a quantity of aqueous solution containing 1.75 mmol KCl and 0.25 mmol KI (molar ratio was set as 7:1) was further slowly dropped and stirred for 3 h at room temperature. Finally, the precipitate was collected, washed with deionized water for several times and dried at 80 °C for 12 h in air. The 20% I-BiOCl/I-BiOBr sample (the molar percentage ratio of I-BiOCl to I-BiOBr was 20%) was denoted as S20%. Similarly, S10%, S30% and S40% samples were also prepared according to the above-mentioned process.

As reference, pure BiOCl and BiOBr were also obtained without adding KI in the process of preparation. Moreover, pure BiOI was fabricated by Bi(NO<sub>3</sub>)<sub>3</sub> and KI.

### 2.2. Characterization

X-ray diffraction (XRD) analysis was performed on a BRUKER D8 ADVANCE X-ray diffractometer equipped with a Cu Ka radiation source and a scanning speed of 3°/min. The UV-vis diffuse reflectance spectra (DRS) measurements were carried out using a PGGENERAL TU-1901 UV-vis spectrophotometer to observe their optical properties. The analysis range was from 200 to 800 nm with BaSO<sub>4</sub> as a reference standard. The morphology of the samples was observed by scanning electron microscopy (SEM) on a FEI Sirion200 with a scanning voltages of 5.00 kV (USA). For the transmission electron microscopy (TEM) and high-resolution TEM (HRTEM) images were taken using a JEOL-2011 transmission electron microscope operated at 200 kV (Japan). The Brunauer-Emmett-Teller (BET) surface area measurements were collected on a Quantachrome NOVA2000 instrument at liquid nitrogen temperature (77.3 K). X-Ray photoelectron spectroscopy (XPS) was carried out on a Thermo

Fisher Scientific Escalab 250 instrument with Al K $\alpha$  source operated at 150 W. Energy dispersive X-ray spectrometer (EDS) was analyzed on a FEI Sirion200 scanning electron microscope operated at a scanning voltages of 5.00 kV (USA).

### 2.3. Photocatalytic activity measurements

Photocatalytic activities of the samples were evaluated by degrading methyl orange (MO) and phenol under visible light irradiation ( $\lambda > 400$  nm). The visible light source was provided by a 500 W Xe lamp coupled with a 400 nm cutoff filter. In each experiment, 0.10 g of catalyst was uniformly dispersed into 50 mL MO (or phenol) solution (10 mg/L). Prior to illumination, the suspension was stirred in the dark for 30 min to reach adsorption-desorption equilibrium between the photocatalyst and the solution. At irradiation time intervals of 10 min (MO) or 1 h (phenol), about 2.5 mL of the suspension was taken out and then centrifuged to remove the photocatalyst particles. Subsequently, the MO solution was analyzed with a 722s spectrophotometer at 464 nm with deionized water as a reference sample. Differently, the absorbance spectra of phenol solutions were analyzed by a TU-1901 UV-vis spectrophotometer using deionized water as a reference sample.

### 2.4. Photoelectrochemical measurements

The photocurrent measurements were performed on a CHI660E Electrochemical Workstation (Chenhua Instruments Co., Shanghai, China) in a standard three-electrode experimental system. The prepared series photoelectrodes, Ag/AgCl (3.0 M KCl), and Pt electrode acted as the working, reference, and counter electrodes, respectively. The visible light irradiation proceeded by a 500 W Xe lamp with a 400 nm cutoff filter. The variations of the photoinduced current intensity with time were measured by controlling the cycle light on and off. The Mott-Schottky curves were collected under the same conditions without the Xe lamp irradiation. All of the measurements were carried out in phosphate buffered saline contained 0.1 M Na<sub>2</sub>HPO<sub>4</sub> and 0.1 M NaH<sub>2</sub>PO<sub>4</sub> aqueous solution at ambient temperature.

Surface photovoltage (SPV) spectroscopy was measured on a TLS-SPV530 spectrometer (Zolix instruments Co., Beijing, China). Monochromatic light was obtained by passing the light from a 500 W Xe lamp through a double prism monochromator. The slit width of entrance and exit was 1 mm. A lock-in amplifier, synchronized with a light chopper was employed to amplify the photovoltage signal. The range of modulating frequency was set from 20 to 70 Hz. The spectral resolution was fixed as 1 nm.

## 3. Results and discussion

### 3.1. Characterization

#### 3.1.1. Crystal structure

The phase and crystallinity of the as-synthesized samples were measured by XRD analysis. Fig. 1 shows that pure BiOBr exhibited high intensity peaks assigning to standard tetragonal BiOBr (JCPDS File NO. 09-0393). After doping with little amount of I<sup>−</sup> ions, the (102) and (110) peaks had slight shift to lower angle region for I-BiOBr, suggesting that I<sup>−</sup> ions with larger ionic radius were successfully incorporated into the BiOBr lattice by replacing a portion of Br<sup>−</sup> ions with smaller ionic radius [41]. The similar peak shift phenomenon was also presented in I-BiOCl in comparison with pure BiOCl (JCPDS File NO. 06-0249). It should be noted that no peak of BiOI could be found in I-BiOBr and I-BiOCl, indicating that BiOI impurity could not be formed in the preparation process of I-BiOBr and I-BiOCl [31,39]. When quantity of I-BiOCl was loaded on the surface of I-BiOBr substrate, a mixed diffraction peaks of I-BiOCl and

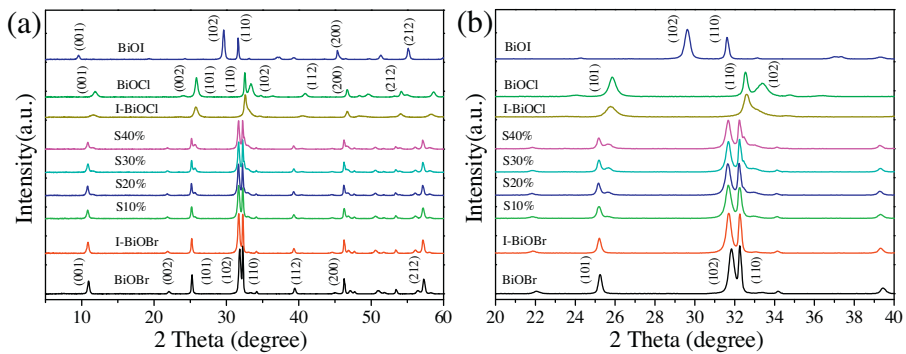


**Fig. 1.** XRD (a) and (b) enlarged XRD patterns of BiOBr, I-BiOBr, S10%, S20%, S30%, S40%, I-BiOCl, BiOCl and BiOI.

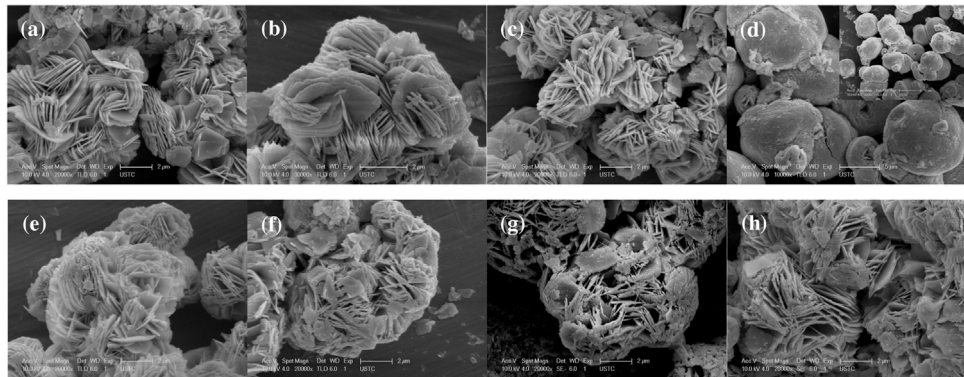


**Fig. 2.** SEM images of (a) BiOBr, (b) I-BiOBr, (c) BiOCl, (d) I-BiOCl, (e) S10%, (f) S20%, (g) S30% and (h) S40%.

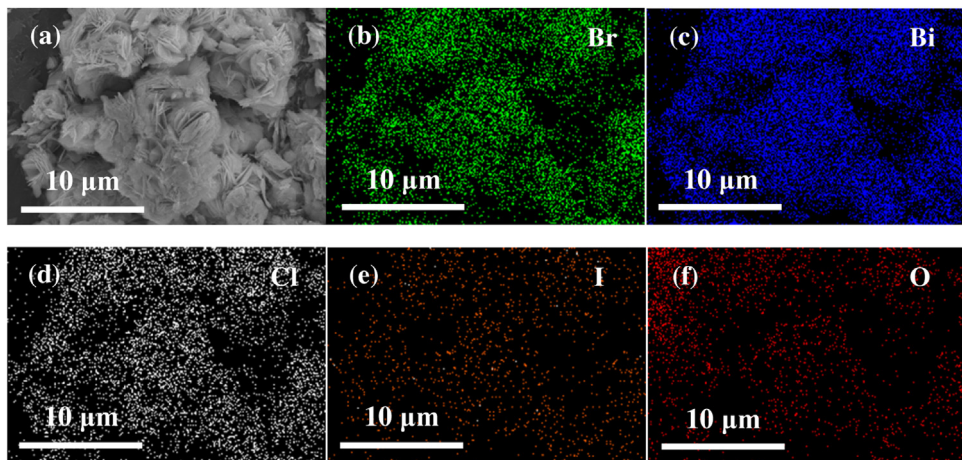


**Fig. 3.** EDS mapping of S20% composite: (a) SEM image, (b) Br, (c) Bi, (d) Cl, (e) I and (e) O.

I-BiOBr were presented in I-BiOCl/I-BiOBr system. With increasing the amount of I-BiOCl, their peak intensities gradually increased while those of I-BiOBr decreased. On the whole, the peak intensities of I-BiOCl were still much weak in all of the I-BiOCl/I-BiOBr composites owing to the low loading contents.

### 3.1.2. Morphology

Fig. 2 shows the SEM images of the various samples. Pure BiOBr (Fig. 2a) and I-BiOBr (Fig. 2b) had the similar hierarchical microflower morphology composed of nanosheets. The morphology of I-BiOCl (Fig. 2d) obviously changed to microsphere from the microflower structure of BiOCl (Fig. 2c) due to large contents of doped I<sup>-</sup> ions. Compared to I-BiOBr, many I-BiOCl nanosheets

covered on the surface of I-BiOBr microflowers, which facilitates the generation of I-BiOCl/I-BiOBr composites. Additionally, More I-BiOCl nanosheets were produced with increasing their loading amounts on I-BiOBr microflowers (Fig. 2e–h).

The surface element dispersion states of S20% composite were measured by powerful EDS mapping technology. Fig. 3 clearly revealed that Br, Bi, Cl, I and O elements were uniformly distributed throughout the S20% sample, respectively. As for the dopant of I<sup>-</sup> ions, the signal intensity was not high (Fig. 3e), suggesting that the content of I element was low in S20% sample.

Moreover, the BET surface areas of as-prepared samples were tested and calculated to be 12.71, 9.51, 11.17, 7.30, 8.97, 9.43, 11.34 and 8.67 m<sup>2</sup>/g for the BiOBr, I-BiOBr, BiOCl, I-BiOCl, S10%, S20%,

S30% and S40% samples, respectively. The similar BET surface areas of all the samples indicate it will not be the main factor for affecting the photocatalytic performance of different samples.

### 3.1.3. Heterostructure interface

To ensure the interface generation between I-BiOCl and I-BiOBr, the TEM and HRTEM images of S20% composite were given in Fig. 4. As comparison, the TEM and HRTEM images of the single BiOCl, I-BiOCl, BiOBr and I-BiOBr were also presented. It can be seen that BiOCl (Fig. 4b) and I-BiOCl (Fig. 4d) had the same interlayer distance of 0.173 nm, corresponding to the (202) facet of BiOCl. Moreover, BiOBr (Fig. 4f) and I-BiOBr (Fig. 4h) displayed the same facet distance of 0.144 nm, originating from the (204) facet of BiOBr. That is, the crystal structures of I-BiOCl and I-BiOBr could not be obviously affected by the little amount of doped I<sup>−</sup> ions. As for I-BiOCl/I-BiOBr heterojunction, its microplate structure of S20% (Fig. 4i) was consistent with the SEM observation. The HRTEM image of S20% shown in Fig. 4j presents that there existed two sets of fringes with the interlayer distances of 0.173 and 0.144 nm, corresponding to the (202) plane of I-BiOCl and the (204) plane of I-BiOBr. This result demonstrates that I-BiOCl/I-BiOBr heterojunction was successfully built between I-BiOCl and I-BiOBr phases in S20% sample. The tightly touched I-BiOCl/I-BiOBr interface will rapidly separate the photocharges induced by visible light on I-BiOCl/I-BiOBr sample.

### 3.1.4. Surface element composition

To investigate the surface chemical compositions and valence states, BiOCl, BiOBr and S20% samples were characterized by XPS. All the peak positions were calibrated by C as reference (284.7 eV). As shown in Fig. 5(a), S20% sample was composed of Bi, O, Br, Cl and I peaks. Their corresponding high-resolution XPS spectra were further displayed in Fig. 5(b)–(f), respectively. Fig. 5(b) shows that two strong peaks with binding energies of 164.8 and 159.5 eV corresponded to the Bi 4f<sub>5/2</sub> and Bi 4f<sub>7/2</sub> [42,43], indicating that the chemical valence of Bi element was +3. The O 1s spectrum was also composed of two peaks after fitting processing. One peak locating around 530.2 eV belonged to crystal O of the samples [44], the other one with higher binding energy of 532.0 eV could be assigned to mixed contributions from the hydroxyl groups [45] adhered on the surface of the samples (Fig. 5c). Moreover, the peaks of Br 3d (Fig. 5d) were associated with binding energy of 70.1 and 69.1 eV, corresponding to Br 3d<sub>3/2</sub> and Br 3d<sub>5/2</sub> [46,47]. As for Cl 2p element (Fig. 5e), Cl 2p<sub>3/2</sub> and Cl 2p<sub>1/2</sub> peaks owned 198.0 and 199.6 eV binding energies, which indicates that the valence state of Cl was −1 in the BiOCl and S20% samples [48]. The most important characteristic peaks lied in the doped I element, as shown in Fig. 5(f). The I 3d peak deconvoluted into two peaks at about 630.9 and 619.4 eV and corresponded to I 3d<sub>3/2</sub> and I 3d<sub>5/2</sub>, affirming the valence state of I was −1 [25]. As a result, the chemical compositions and valence states presented in the XPS data coincided with those in the samples, which suggest I-BiOCl/I-BiOBr heterostructure was successfully constructed through deposition-precipitation process along with the I<sup>−</sup> ion doping step. It is worth noting that, the peak positions and intensities of Bi, O, Br and Cl elements in S20% had little difference with the single BiOCl and BiOBr, which was probably due to the little amount of doped I<sup>−</sup> ions.

### 3.1.5. Light absorption

To determine the band gap energies of the as-prepared samples, their UV–vis reflectance absorption spectra were provided in Fig. 6. It can be seen from Fig. 6a that pure BiOCl absorbed ultraviolet light with edge about 350 nm, so it is a typical wideband-gap semiconductor. Obviously, the doped I<sup>−</sup> ions greatly extended the light absorption edge of I-BiOCl to 530 nm. Similarly, the doped I<sup>−</sup> ions also expanded the visible light absorption range of I-BiOBr to 520 nm. That is, I<sup>−</sup> ions formed impurity levels in I-BiOCl and

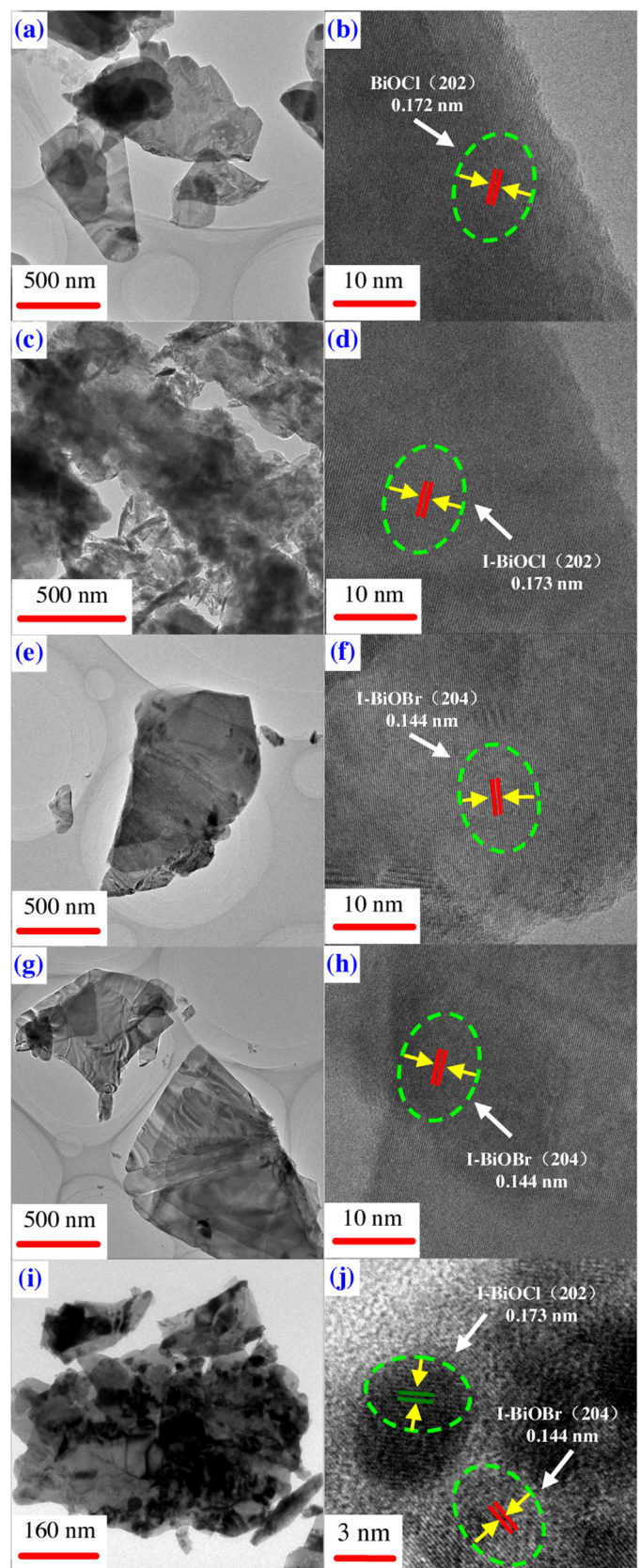


Fig. 4. TEM and HRTEM images of (a), (b) BiOCl, (c), (d) I-BiOCl, (e), (f) BiOBr, (g), (h) I-BiOBr and (i), (j) S20% composite.

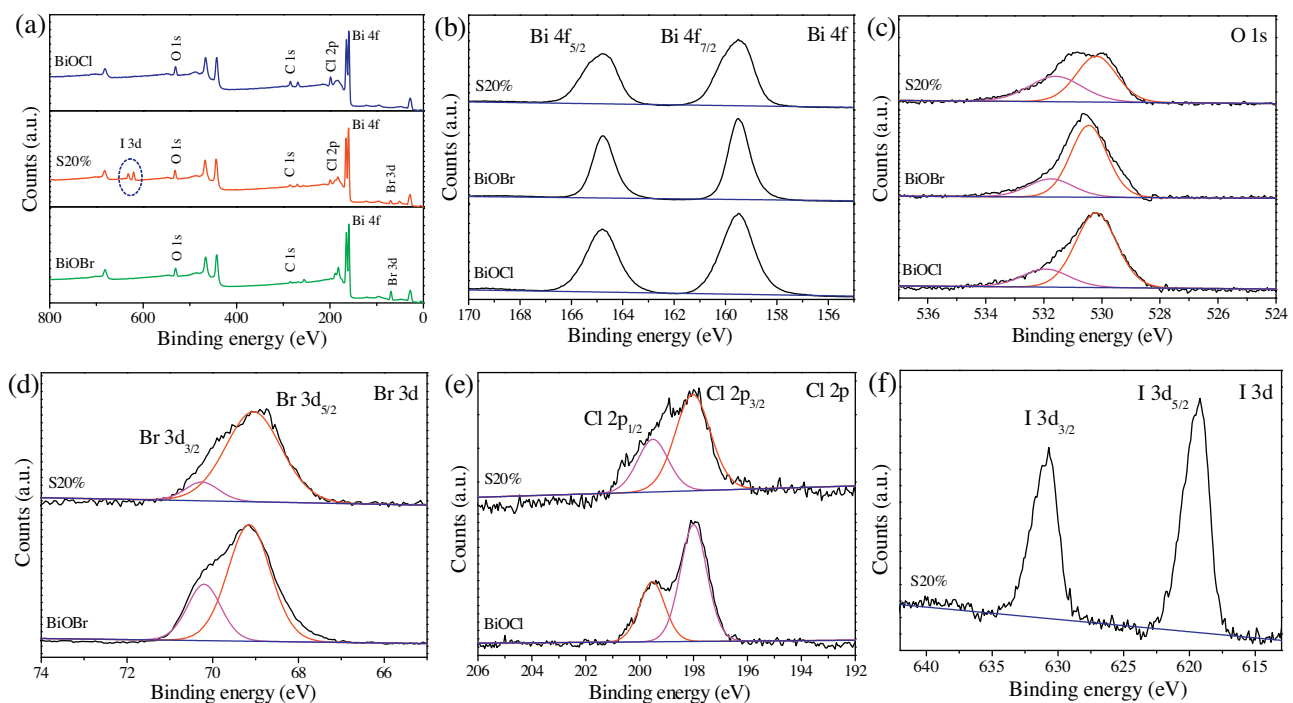


Fig. 5. XPS spectra of BiOBr, BiOCl and S20% sample: (a) survey spectra, (b) Bi 4f, (c) O 1s, (d) Br 3d, (e) Cl 2p and (f) I 3d.

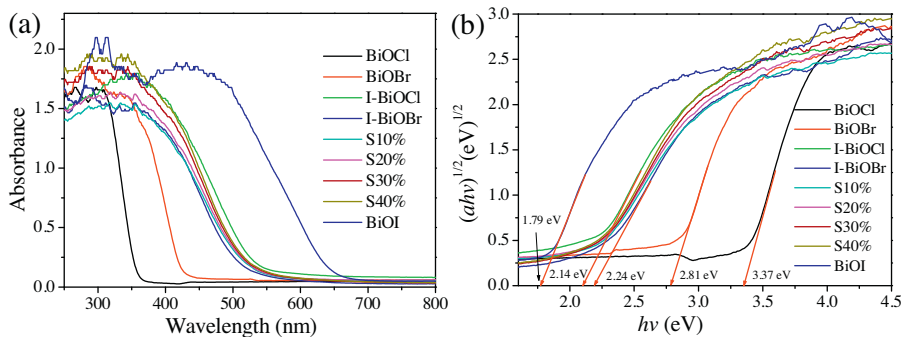


Fig. 6. (a) UV-vis diffuse reflectance spectra and (b) band gap energies of the samples.

I-BiOBr crystals, which narrowed their band-gap energies [49–51]. Due to the doping contents of  $I^-$  ions in I-BiOCl was larger than that in I-BiOBr, the changes of light absorption ranges was much more remarkable from BiOCl to I-BiOCl than that from BiOBr to I-BiOBr. After assembling I-BiOBr with little amount of I-BiOCl, the light absorption ranges of I-BiOCl/I-BiOBr were situated between I-BiOCl and I-BiOBr. With increasing the loading amount of I-BiOCl from 10 to 40%, the light absorption edges of I-BiOCl/I-BiOBr slightly expanded, which ensures the excellent visible light absorption of I-BiOCl/I-BiOBr.

Based on these results, the band gap energies of all the samples were estimated according to Formula (1) [17]:

$$\alpha h\nu = A(h\nu - E_g)^{n/2} \quad (1)$$

where  $\alpha$ ,  $h$ ,  $\nu$ ,  $A$  and  $E_g$  stand for absorption coefficient, Planck constant, light frequency, a constant and band gap energy, respectively. Moreover, the  $n$  value is determined by the type of optical transition of a semiconductor ( $n = 1$  for a direct transition and  $n = 4$  for an indirect transition). According to reported literatures, the  $n$  value of BiOX was 4 [52]. Thus, the corresponding  $E_g$  values of BiOBr, I-BiOBr, BiOCl, I-BiOCl and BiOI were calculated to be about 2.81, 2.24, 3.37, 2.14 and 1.79 eV, respectively, as shown in Fig. 6b. This

result obviously illustrates that the decrease in  $E_g$  values of BiOBr was 0.57 eV but that of BiOCl was 1.23 eV through doping  $I^-$  ions. The  $E_g$  values reduce of BiOBr and BiOCl provided the necessary energy structure matching for transforming type-I BiOCl/BiOBr to type-II I-BiOCl/I-BiOBr.

### 3.1.6. Flat band potential

To further evaluate the effect of doped  $I^-$  ions on the energy band structures of BiOCl and BiOBr samples, the Mott-Schottky curves were measured and the results were shown in Fig. 7. The positive slope of the  $C^{-2}-E$  plot indicates that BiOBr, I-BiOBr, BiOCl and I-BiOCl belonged to  $n$ -type semiconductors [53]. The corresponding flat band potentials ( $V_{fb}$ ) were  $-0.80$ ,  $-0.80$ ,  $-0.91$  and  $-0.91$  V vs Ag/AgCl at pH 6.8 for BiOBr, I-BiOBr, BiOCl and I-BiOCl. If the above values were converted to normal hydrogen electrode (NHE) potential, the  $V_{fb}$  values were  $-0.60$ ,  $-0.60$ ,  $-0.71$  and  $-0.71$  V vs NHE at pH 6.8 [54], respectively. As reported, the conduction band potential ( $E_{CB}$ ) was very close to the  $V_{fb}$  [54] for  $n$ -type semiconductors, it is concluded that the  $E_{CB}$  values of BiOBr, I-BiOBr, BiOCl and I-BiOCl were  $-0.60$ ,  $-0.60$ ,  $-0.71$  and  $-0.71$  V vs NHE. That is, the doped  $I^-$  ions could not change the  $V_{fb}$  as well as the  $E_{CB}$  values of BiOBr and BiOCl.

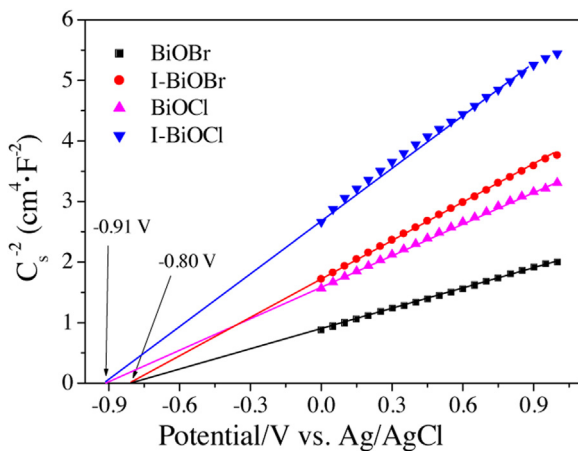


Fig. 7. Mott-Schottky plot of the as-prepared samples in phosphate buffered saline aqueous solution ( $\text{pH} = 6.8$ ).

Hitherto, we are intensively interested in the valence band potential ( $E_{VB}$ ) of the BiOBr, I-BiOBr, BiOCl and I-BiOCl, since a complete energy band structure of a semiconductor included both the  $E_{CB}$  and the  $E_{VB}$  values. In view of the above consideration, the  $E_{VB}$  values were also calculated according to the formula (2) [55]:

$$E_{CB} = E_{VB} - E_g \quad (2)$$

Therefore, the  $E_{VB}$  values were estimated to be 2.21, 1.64, 2.66 and 1.43 V for BiOBr, I-BiOBr, BiOCl and I-BiOCl, respectively. In order to easily understand the energy band structure change from BiOCl/BiOBr I-BiOCl/I-BiOBr, a schematic diagram was provided in Fig. 8.

Thus, the type-I BiOCl/BiOBr heterostructure has been successfully converted to type-II I-BiOCl/I-BiOBr heterostructure. In the type-I BiOCl/BiOBr system, only BiOBr can be activated by visible light whereas the white BiOCl was inert to visible light. The photocharges can not be efficiently separated via the BiOCl/BiOBr interface. Notably, I-BiOCl/I-BiOBr showed a typical

type-II structure. More importantly, both I-BiOCl and I-BiOBr can be motivated under visible light due to their small band gap energy. The interlaced energy band structure will facilitate the fast separation of photocharges in the novel type-II I-BiOCl/I-BiOBr system.

### 3.2. Photocatalytic activity

The as-prepared novel type-II I-BiOCl/I-BiOBr composites were applied in degrading contaminant models MO and phenol under visible light ( $\lambda > 400 \text{ nm}$ ). As shown in Fig. 9a, the self-photolysis of MO was not observable, suggesting that MO was stable under visible light. As reference sample,  $\text{TiO}_2$  (P25), BiOCl and BiOBr displayed very weak activity for MO degradation due their large band gap energies. After doping amount of  $\text{I}^-$  ions, MO could be degraded about 30% and 45% by I-BiOCl and I-BiOBr. This ensures the significant doping effect of  $\text{I}^-$  ions in BiOX system. More importantly, the coupling of I-BiOCl and I-BiOBr further demonstrated outstanding activity improvement for MO removal. For example, S20% sample eliminated about of 95% MO with 40 min irradiation of visible light. The other S10%, S30% and S40% composites also presented excellent activity in comparison with I-BiOCl and I-BiOBr. This result completely ensures the remarkable heterojunction interface effect of I-BiOCl/I-BiOBr. Moreover, the loading amount of I-BiOCl on the surface of I-BiOBr dramatically affected the activity of I-BiOCl/I-BiOBr. In other words, the activity rose firstly and then decreased with increasing the amount of I-BiOCl. When the loading amount of I-BiOCl was controlled at 20%, I-BiOCl/I-BiOBr obtained the highest activity for MO degradation. Encouraged by the above exciting results, phenol degradation over the I-BiOCl/I-BiOBr composites was also carried out. The excellent activity of I-BiOCl/I-BiOBr composites (Fig. 9c) was also found in comparison with the reference samples, such as  $\text{TiO}_2$  (P25), BiOCl, BiOBr, I-BiOCl and I-BiOBr. The activity change of the samples in phenol degradation was the same as that in MO degradation, which confirms the superiority of the type-II I-BiOCl/I-BiOBr heterostructure.

In order to further understand the reaction kinetics of MO and phenol degradation, the pseudo-first-order rate constant was

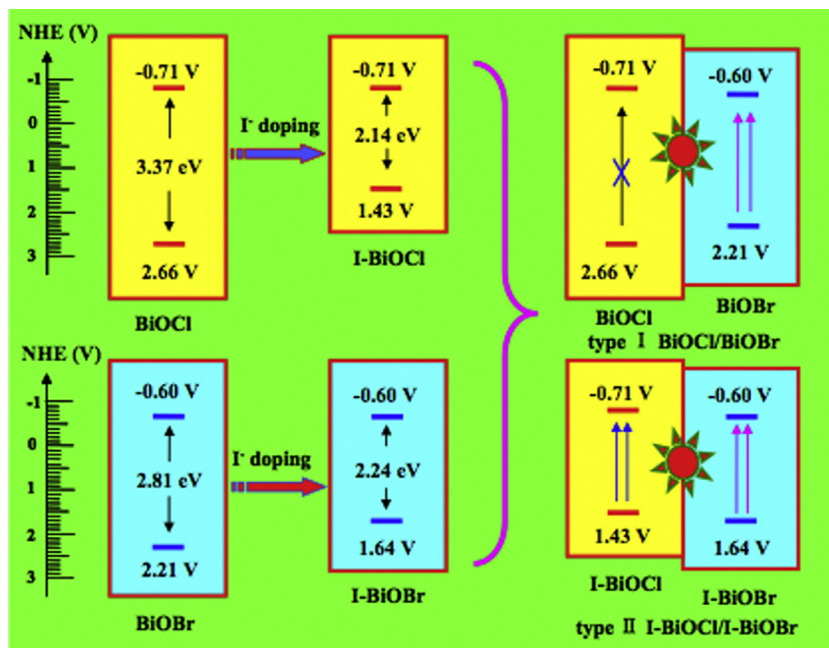
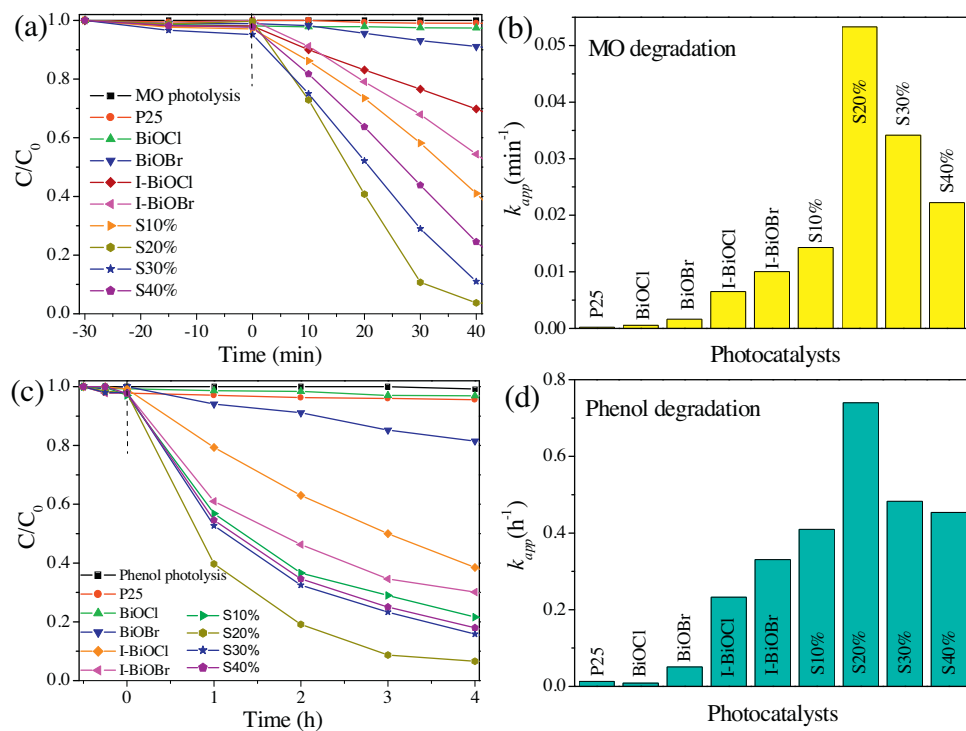
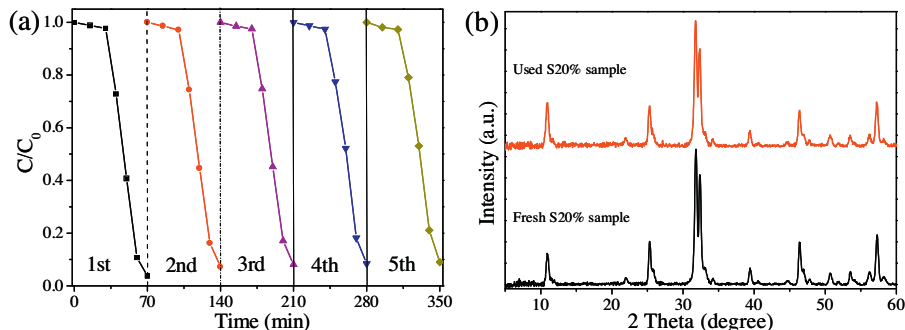


Fig. 8. The energy band structure of type-II I-BiOCl/I-BiOBr composite induced by the  $\text{I}^-$  ions doping.



**Fig. 9.** Photocatalytic activities (a), (c) and the corresponding  $k_{app}$  values (b), (d) of different photocatalysts for MO and phenol degradation under visible light ( $\lambda > 400$  nm).



**Fig. 10.** (a) Cycling runs of S20% sample for the degradation of MO under visible light ( $\lambda > 400$  nm) and (b) XRD patterns of the fresh and used S20% sample for MO degradation under visible light ( $\lambda > 400$  nm).

calculated according to the Langmuir-Hinshelwood kinetics model, expressed as the following Eq. (3) [56]:

$$\ln \frac{C_0}{C} = k_{app} t \quad (3)$$

where  $k_{app}$  is the pseudo-first-order rate constant ( $\text{min}^{-1}$  or  $\text{h}^{-1}$ ),  $C_0$  is the original MO and phenol concentration (10 mg/L),  $C$  is the concentration at reaction time  $t$  (mg/L). The  $k_{app}$  values of MO and phenol degradation are shown in Fig. 9b and d, respectively. It can be seen that the  $k_{app}$  values of I-BiOCl/I-BiOBr changed remarkably and the maximal  $k_{app}$  values were obtained over S20% sample for MO ( $0.058 \text{ min}^{-1}$ ) and phenol ( $0.74 \text{ h}^{-1}$ ) degradation under visible light. The activity enhancement of I-BiOCl/I-BiOBr resulted from the highly efficient separation efficiency of photocharges originating from the feasible type-II energy band structure. Fig. 10a reveals the cycling stability of S20% sample used for degrading MO. It shows that S20% sample still kept excellent photocatalytic activity after 5 times cycling usage under visible light ( $\lambda > 400$  nm). This result indicates that the novel I-BiOCl/I-BiOBr is a kind of stable composite for organic contaminant removal. The corresponding XRD result

(Fig. 10b) also ensures the crystal stability of S20% sample after 5 times cycling experiment in the photocatalytic process.

### 3.3. Active species detection

Generally, the degradation of organic contaminants is accomplished relying on the reactive species generated on the surface of photocatalysts. Thus, many commonly used scavengers were applied as molecular probes for detecting the kinds of reactive species in I-BiOCl/I-BiOBr composite. In detail, *tert*-butyl alcohol (TBA), benzoquinone (BQ) and ethylenediamine tetraacetic acid disodium salt (EDTA-2Na) [57–61] with the same concentration of 0.1 mM in the MO and phenol solutions were employed for testing the hydroxyl radicals ( $\cdot\text{OH}$ ), superoxide radical ( $\cdot\text{O}_2^-$ ) and holes ( $\text{h}^+$ ), respectively. The result (Fig. 11) shows that the activity of S20% sample decreased significantly after adding BQ, EDTA-2Na and TBA, suggesting that  $\cdot\text{O}_2^-$ ,  $\text{h}^+$  as well as  $\cdot\text{OH}$  acted as reactive species in the I-BiOCl/I-BiOBr system under visible light for MO and phenol degradation. The kinds of reactive species provide necessary

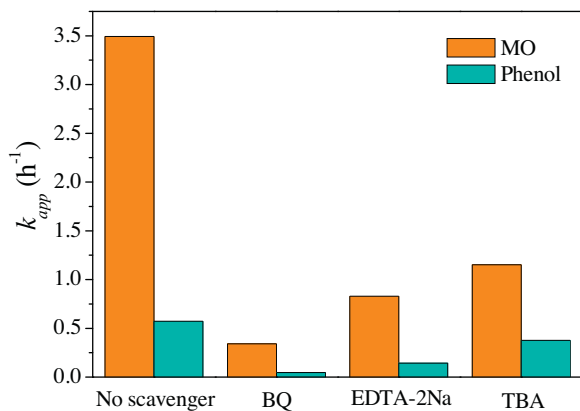


**Fig. 11.**  $k_{app}$  values of MO and phenol degradation over S20% sample after adding different scavengers.

information to discuss the separation process of photocharges in I-BiOCl/I-BiOBr system.

### 3.4. Separation efficiency of photocharges

The excellent activity of I-BiOCl/I-BiOBr motivated us to further investigate the separation efficiency of photocharges under visible light. In view of the intensive relation between the separation of photocharges and the transient photocurrent intensity, the photocurrent responses of all the samples were measured by using electrochemical workstation under the visible light irradiation ( $\lambda > 400 \text{ nm}$ ). As shown in Fig. 12a, the photocurrent signals were about zero without light exposure while kept a constant value as long as the light was turned on, which indicates that the as-prepared samples presented separation ability of photocharges. Further analysis displays that different photocurrent intensities were obtained for the various samples. Generally, the photocurrent intensity was determined by the separation efficiency of photocharges, i.e. the higher photocurrent intensity corresponded to higher separation efficiency of photocharges. Compare to the single pure BiOCl and BiOBr, the doped I-BiOCl and I-BiOBr had higher photocurrent responses, showing the enhanced separation efficiency of electrons and holes. Moreover, the I-BiOCl/I-BiOBr composites, especially for S20% sample, were of strong photocurrent responses, suggesting the separation efficiency of photocharges intensively strengthened. In relation to the activity changes of the samples (Fig. 9), the photocurrent intensity exhibited the same variation trend. The above results assured that the I-BiOCl/I-BiOBr heterojunction interface promoted the separation efficiency of photocharges, which further heightened the photocatalytic activity under visible light.

In addition, surface photovoltage (SPV) spectrum was also employed to further detect the transfer direction of photocharges for illustrating the separation efficiency. This result will give us necessary information to discuss the photocatalytic mechanism of photocatalyst [62,63]. The positive SPV responses (Fig. 12b) indicate that the photogenerated positive holes moved to the surface meanwhile the photogenerated electrons shifted oppositely to the interior of the photocatalysts. As for pure BiOCl, very weak SPV signal originating from the band-to-band transition was found in the UV region, suggesting little excess photocharges were generated owing to the fast recombination rate. After doping with I<sup>-</sup> ions, weak SPV intensity in the 330–470 nm region was appeared due to the sub-band transition. Comparatively, pure BiOBr presented strong SPV intensity in the region of 300–450 nm because a great deal of positive holes aggregated on the surface of BiOBr and electrons quickly transferred to the inner of BiOBr. Similarly, a weak SPV peak of I-BiOBr between 430 and 470 nm was displayed due to the sub-band transition of doped I<sup>-</sup> ions. The narrowed band gap of I-BiOBr inevitably induced the fast recombination of photocharges. When little amount of I-BiOCl was loaded on the surface of I-BiOBr, enhanced SPV response was presented in comparison with the I-BiOBr and I-BiOCl, which reflects the improved separation efficiency of photocharges. Under this condition, more positive holes were able to move to the surface through the I-BiOCl/I-BiOBr interface. Considering the energy band structure of I-BiOCl/I-BiOBr composite, the holes on the valence band of I-BiOBr quickly transferred to that of I-BiOCl and then aggregated on the surface. Consequently, the SPV response of I-BiOCl/I-BiOBr was strengthened. In a word, the type-II I-BiOCl/I-BiOBr composite demonstrated excellent separation efficiency of photocharges under visible light.

### 3.5. Electron-hole separation pathway

On the basis of the above-mentioned energy band structure of type-II I-BiOCl/I-BiOBr and kinds of reactive species taking part in the photocatalytic process, a probable charge transfer mechanism of the enhanced photocatalytic activity of novel I-BiOCl/I-BiOBr composites was proposed here. As shown in Fig. 13, due to the I<sup>-</sup> ions doping, both I-BiOCl and I-BiOBr components were stimulated under visible light irradiation ( $\lambda > 400 \text{ nm}$ ). The electrons transferred from the I<sup>-</sup> ions impurity levels to the corresponding conduction bands. Due to the low contents of I-BiOCl in I-BiOCl/I-BiOBr composite, only little amount of electrons on the conduction band of I-BiOCl would smoothly move to that of I-BiOBr through the heterojunction interface. After that, the electrons with redox potential of  $-0.60 \text{ V}$  reacted with the adsorbed surface O<sub>2</sub> to form  $\bullet\text{O}_2^-$  radicals ( $E^0(\text{O}_2/\bullet\text{O}_2^-) = -0.33 \text{ V/NHE}$ ) [64,65] that degraded MO and phenol to the final products. In addition, partial  $\bullet\text{O}_2^-$  radicals simultaneously reacted with H<sup>+</sup> to generate another kind of

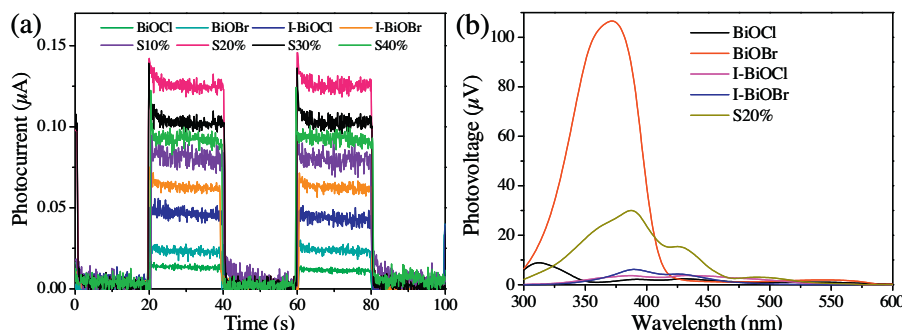


**Fig. 12.** (a) Transient photocurrent responses of different samples in phosphate buffered saline aqueous solution under visible light irradiation and (b) surface photovoltage signals of different samples.

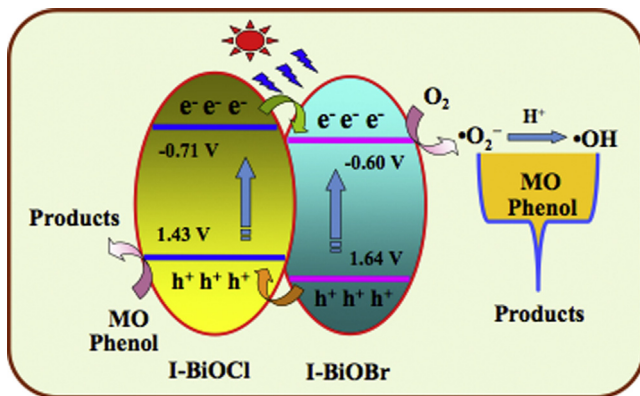


Fig. 13. Schematic illustration of the charge transfer process of the novel type-II I-BiOCl/I-BiOBr under visible light irradiation ( $\lambda > 400$  nm).

radical  $\cdot\text{OH}$ . The formed  $\cdot\text{OH}$  also eliminated the MO and phenol efficiently. During the electron transfer process, a great deal of holes on the valence band of I-BiOBr shifted to that of I-BiOCl. The valence band potential of I-BiOCl was 1.43 V, more negative than that of  $\cdot\text{OH}$  formation potential ( $E^0(\cdot\text{OH}, \text{H}^+/\text{H}_2\text{O}) = 2.72$  V/NHE) [66]. This suggests that holes could directly degrade MO and phenol in the photocatalytic process. The important hole trapping role of loaded I-BiOCl in the novel I-BiOCl/I-BiOBr system was also ensured by the activity change of I-BiOCl/I-BiOBr composite under the condition of N<sub>2</sub> atmosphere. The  $k_{app}$  value of MO degradation decreased from 0.058 to 0.047 min<sup>-1</sup> after letting N<sub>2</sub> into the reactor. This result indicates that when the O<sub>2</sub> contents was reduced, I-BiOCl/I-BiOBr still kept high activity due to the fast separation process through quickly transferring the holes from I-BiOBr to I-BiOCl. In summary, the novel I-BiOCl/I-BiOBr composite exhibited excellent separation efficiency of photocharges and dramatic visible light photocatalytic activity. This work afforded a potential method to construct novel type-II semiconductor heterojunction interface *via* energy band engineering strategy utilizing the prominent ion doping effect.

#### 4. Conclusions

Novel type-II I-BiOCl/I-BiOBr composite was successfully assembled through a facile deposition-precipitation method. The matching energy band structure of I-BiOCl/I-BiOBr was achieved by the remarkable valence band elevation employing I<sup>-</sup> ions as dopants. I-BiOCl/I-BiOBr exhibited largely enhanced photocatalytic activity for MO and phenol removal under visible light ( $\lambda > 400$  nm). The narrowed energy band gap of I-BiOCl/I-BiOBr guaranteed the efficient utilization of visible light meanwhile the I-BiOCl/I-BiOBr interface facilitated the high separation of photocharges. The energy band engineering offered a potential way to construct novel type-II heterojunction composite through transforming the original type-I heterojunction composite.

#### Acknowledgements

This work was financially supported by the Natural Science Foundation of China (51472005, 51272081), the Natural Science Foundation of Educational Committee of Anhui Province (KJ2015A027, gxyqZD2016413, gxyqZD2016414), State Key Laboratory of Structural Chemistry (20160014) and Innovation Team of Design and Application of Advanced Energetic Materials.

#### References

- R. Asahi, T. Morikawa, T. Ohwaki, K. Aoki, Y. Taga, Visible-light photocatalysis in nitrogen-doped titanium oxides, *Science* 293 (2001) 269–271.
- A. Houas, H. Lachheb, M. Ksibi, E. Elaloui, C. Guillard, J.M. Herrmann, Photocatalytic degradation pathway of methylene blue in water, *Appl. Catal. B: Environ.* 31 (2001) 145–157.
- W.S. Kuo, P.H. Ho, Solar photocatalytic decolorization of dyes in solution with TiO<sub>2</sub> film, *Dyes Pigm.* 71 (2006) 212–217.
- S.Y. Ouyang, H. Tong, N. Umezawa, J.Y. Cao, P. Li, Y.P. Bi, Y.J. Zhang, J.H. Ye, Surface-alkalinization- induced enhancement of photocatalytic H<sub>2</sub> evolution over SrTiO<sub>3</sub>-based photocatalysts, *J. Am. Chem. Soc.* 134 (2012) 1974–1977.
- X.B. Chen, S.H. Shen, L.J. Guo, S.S. Mao, Semiconductor-based photocatalytic hydrogen generation, *Chem. Rev.* 110 (2010) 6503–6570.
- X. Zong, H.J. Yan, G.P. Wu, G.J. Ma, F.Y. Wen, L. Wang, C. Li, Enhancement of photocatalytic H<sub>2</sub> evolution on CdS by loading MoS<sub>2</sub> as cocatalyst under visible light irradiation, *J. Am. Chem. Soc.* 130 (2008) 7176–7177.
- X.G. Han, Q. Kuang, M.S. Jin, Z.X. Xie, L.S. Zheng, Synthesis of titania nanosheets with a high percentage of exposed (001) facets and related photocatalytic properties, *J. Am. Chem. Soc.* 131 (2009) 3152–3153.
- J.R. Jin, Y.J. Wang, T. He, Preparation of thickness-tunable BiOCl nanosheets with high photocatalytic activity for photoreduction of CO<sub>2</sub>, *RSC Adv.* 5 (2015) 100244–100250.
- F. Chen, H.Q. Liu, S. Bagwasi, X.X. Shen, J.L. Zhang, Photocatalytic study of BiOCl for degradation of organic pollutants under UV irradiation, *J. Photochem. Photobiol. A: Chem.* 215 (2010) 76–80.
- V. Kandavelu, H. Kastien, K.R. Thampi, Photocatalytic degradation of isothiazolin-3-ones in water and emulsion paints containing nanocrystalline TiO<sub>2</sub> and ZnO catalysts, *Appl. Catal. B: Environ.* 48 (2004) 101–111.
- S.Y. Choi, Y.J. Kim, M.H. Jung, A.K. Chakraborty, D. Jung, W.I. Lee, Heterojunctioned BiOCl/Bi<sub>2</sub>O<sub>3</sub> a new visible light photocatalyst, *J. Catal.* 262 (2009) 144–149.
- D. Yue, D.M. Chen, Z.H. Wang, H. Ding, R.L. Zong, Y.F. Zhu, Enhancement of visible photocatalytic performances of a Bi<sub>2</sub>MoO<sub>6</sub>-BiOCl nanocomposite with plate-on-plate heterojunction structure, *Phys. Chem. Chem. Phys.* 16 (2014) 26314–26321.
- M.L. Sun, Q.H. Zhao, C.F. Du, Z.L. Liu, Enhanced visible light photocatalytic activity in BiOCl/SnO<sub>2</sub>: heterojunction of two wide band-gap semiconductors, *RSC Adv.* 5 (2015) 22740–22752.
- Y.X. Guo, H.W. Huang, Y. He, N. Tian, T.R. Zhang, P.K. Chu, Q. An, Y.H. Zhang, *In situ* crystallization for fabrication of a core-satellite structured BiOBr-CdS heterostructure with excellent visible-light-responsive photoreactivity, *Nanoscale* 7 (2015) 11702–11711.
- J. Di, J.X. Xia, S. Yin, H. Xu, L. Xu, Y.G. Xu, M.Q. He, H.M. Li, Preparation of sphere-like g-C<sub>3</sub>N<sub>4</sub>/BiOI photocatalysts *via* a reactable ionic liquid for visible-light-driven photocatalytic degradation of pollutants, *J. Mater. Chem. A* 2 (2014) 5340–5351.
- H.F. Cheng, B.B. Huang, X.Y. Qin, X.Y. Zhang, Y. Dai, A controlled anion exchange strategy to synthesize Bi<sub>2</sub>S<sub>3</sub> nanocrystals/BiOCl hybrid architectures with efficient visible light photoactivity, *Chem. Commun.* 48 (2012) 97–99.
- T.B. Li, G. Chen, C. Zhou, Z.Y. Shen, R.C. Jin, J.X. Sun, New photocatalyst BiOCl/BiOI composites with highly enhanced visible light photocatalytic performances, *Dalton Trans.* 40 (2011) 6751–6758.
- H.W. Huang, X. Han, X.W. Li, S.C. Wang, P.K. Chu, Y.H. Zhang, Fabrication of multiple heterojunctions with tunable visible-light-active photocatalytic reactivity in BiOBr-BiOI full-range composites based on microstructure modulation and band structures, *ACS Appl. Mater. Interfaces* 7 (2015) 482–492.
- S.J. Zhang, J.F. Yang, Microwave-assisted synthesis of BiOCl/BiOBr composites with improved visible-light photocatalytic activity, *Ind. Eng. Chem. Res.* 54 (2015) 9913–9919.
- L. Chen, S.F. Yin, R. Huang, Y. Zhou, S.L. Luo, C.T. Au, Facile synthesis of BiOCl nano-flowers of narrow band gap and their visible-light-induced photocatalytic property, *Catal. Commun.* 23 (2012) 54–57.
- L. Chen, R. Huang, M. Xiong, Q. Yuan, J. He, J. Jia, M.Y. Yao, S.L. Luo, C.T. Au, S.F. Yin, Room-temperature synthesis of flower-like BiOX (X = Cl, Br, I) hierarchical structures and their visible-light photocatalytic activity, *Inorg. Chem.* 52 (2013) 11118–11125.
- L.Q. Ye, Y.R. Su, X.L. Jin, H.Q. Xie, C. Zhang, Recent advances in BiOX (X = Cl, Br and I) photocatalysts: synthesis, modification, facet effects and mechanisms, *Environ. Sci.: Nano* 1 (2014) 90–112.
- S.Y. Choi, Y.J. Kim, M.H. Jung, A.K. Chakraborty, D. Jung, W.I. Lee, Heterojunctioned BiOCl/Bi<sub>2</sub>O<sub>3</sub>: a new visible light photocatalyst, *J. Catal.* 262 (2009) 144–149.
- L. Kong, Z. Jiang, H.H. Lai, R.J. Nicholls, T.C. Xiao, M.O. Jones, P.P. Edwards, Unusual reactivity of visible-light-responsive AgBr-BiOBr heterojunction photocatalysts, *J. Catal.* 293 (2012) 116–125.
- L.Q. Ye, J.Y. Liu, Z. Jiang, T.Y. Peng, L. Zan, Facets coupling of BiOBr-g-C<sub>3</sub>N<sub>4</sub> composite photocatalyst for enhanced visible-light-driven photocatalytic activity, *Appl. Catal. B: Environ.* 142–143 (2013) 1–7.
- Y.H. Ao, K.D. Wang, P.F. Wang, C. Wang, J. Hou, Synthesis of novel 2D-2D p-n heterojunction BiOBr/La<sub>2</sub>Ti<sub>2</sub>O<sub>7</sub> composite photocatalyst with enhanced photocatalytic performance under both UV and visible light irradiation, *Appl. Catal. B: Environ.* 194 (2016) 157–168.
- L. Chen, S.F. Yin, S.L. Luo, R. Huang, Q. Zhang, T. Hong, P.C.T. Au, Bi<sub>2</sub>O<sub>2</sub>CO<sub>3</sub>/BiOI photocatalysts with heterojunctions highly efficient for visible-light treatment of dye-containing wastewater, *Ind. Eng. Chem. Res.* 51 (2012) 6760–6768.
- J. Zhang, J.X. Xia, S. Yin, H.M. Li, H. Xu, M.Q. He, L.Y. Huang, Q. Zhang, Improvement of visible light photocatalytic activity over flower-like

BiOCl/BiOBr microspheres synthesized by reactable ionic liquids, *Colloid Surf. A: Physicochem. Eng. Asp.* 420 (2013) 89–95.

[29] J. Cao, B.Y. Xu, H.L. Lin, B.D. Luo, S.F. Chen, Chemical etching preparation of BiO<sub>x</sub>/BiOBr heterostructures with enhanced photocatalytic properties for organic dye removal, *Chem. Eng. J.* 185–186 (185) (2012) 914–999.

[30] T.B. Li, G. Chen, C. Zhou, Z.Y. Shen, R.C. Jin, J.X. Sun, New photocatalyst BiOCl/BiO<sub>x</sub> composites with highly enhanced visible light photocatalytic performances, *Dalton Trans.* 40 (2011) 6751–6758.

[31] W.D. Wang, F.Q. Huang, X.P. Lin, xBiO<sub>1-x</sub>BiOCl as efficient visible-light-driven photocatalysts, *Scripta Mater.* 56 (2007) 669–672.

[32] K.X. Ren, J. Liu, J. Liang, K. Zhang, X. Zheng, H.D. Luo, Y.B. Huang, P.J. Liu, X.B. Yu, Synthesis of the bismuth oxyhalide solid solutions with tunable band gap and photocatalytic activities, *Dalton Trans.* 42 (2013) 9706–9712.

[33] W.J. Kim, D. Pradhan, B.K. Min, Y. Sohn, Adsorption/photocatalytic activity and fundamental natures of BiOCl and BiOCl<sub>x</sub>I<sub>1-x</sub> prepared in water and ethylene glycol environments, and Ag and Au-doping effects, *Appl. Catal. B: Environ.* 147 (2014) 711–725.

[34] C.D. Wang, H. Qiu, T. Inoue, Q.W. Yao, Electronic structure calculations of I and Mn doped BiOCl with modified Becke-Johnson potential, *Comp. Mater. Sci.* 85 (2014) 138–141.

[35] X.N. Wang, H.C. Chen, H.J. Li, G. Mailhot, W.B. Dong, Preparation and formation mechanism of BiOCl<sub>0.7</sub>I<sub>0.25</sub> nanospheres by precipitation method in alcohol-water mixed solvents, *J. Colloid Interface Sci.* 478 (2016) 1–10.

[36] Y.Q. Lei, G.H. Wang, P.R. Guo, H.C. Song, The Ag-BiOBr<sub>x</sub>I<sub>1-x</sub> composite photocatalyst: preparation, characterization and their novel pollutants removal property, *Appl. Surf. Sci.* 279 (2013) 374–379.

[37] H. Liu, Y. Su, Z. Chen, Z.T. Jin, Y. Wang, Novel 3D flowerlike Au/BiOBr<sub>0.7</sub>I<sub>0.3</sub> composites with highly enhanced visible-light photocatalytic performances, *Sep. Purif. Technol.* 133 (2014) 343–350.

[38] S.W. Lee, I.S. Cho, Y.K. Sohn, Hierarchical BiOBr, AgBr/BiOBr and BiOBr<sub>x</sub>I<sub>1-x</sub> nano-assembled microspheres for photocatalytic methyl orange treatment, *J. Nanosci. Nanotechnol.* 15 (2015) 8362–8369.

[39] Z.C. Yang, F.X. Cheng, X.P. Dong, F.M. Cui, Controllable in situ synthesis of BiOBr<sub>x</sub>I<sub>1-x</sub> solid solution on reduced graphene oxide with enhanced visible light photocatalytic performance, *RSC Adv.* 5 (2015) 68151–68158.

[40] C.R. Zheng, C.B. Cao, Z. Ali, In situ formed Bi/BiOBr<sub>x</sub>I<sub>1-x</sub> heterojunction of hierarchical microspheres for efficient visible-light photocatalytic activity, *Phys. Chem. Chem. Phys.* 17 (2015) 13347–13354.

[41] C.J. Bi, J. Cao, H.L. Lin, Y.J. Wang, S.F. Chen, Tunable photocatalytic and photoelectric properties of I<sup>-</sup>-doped BiOBr photocatalyst: dramatic pH effect, *RSC Adv.* 6 (2016) 15525–15534.

[42] L.Q. Ye, J.N. Chen, L.H. Tian, J.Y. Liu, T.Y. Peng, K.J. Deng, L. Zan, BiO<sub>x</sub> thin film via chemical vapor transport: photocatalytic activity durability, selectivity and mechanism, *Appl. Catal. B: Environ.* 130–131 (2013) 1–7.

[43] L.L. Li, L.H. Ai, C.H. Zhang, J. Jiang, A high impact peer reviewed journal publishing experimental and theoretical work across the breadth of nanoscience and nanotechnology, *Nanoscale* 6 (2014) 4627–4634.

[44] K.M. Jia, H.X. Dai, J.G. Deng, H.J. Zang, H. Arandiyand, S.H. Xie, H.G. Yang, 3DOM BiVO<sub>4</sub> supported silver bromide and noble metals: high-performance photocatalysts for the visible-light-driven degradation of 4-chlorophenol, *Appl. Catal. B: Environ.* 168 (2015) 274–282.

[45] Y.N. Huo, J. Zhang, M. Miao, Y. Jin, Solvothermal synthesis of flower-like BiOBr microspheres with highly visible-light photocatalytic performances, *Appl. Catal. B: Environ.* 111–112 (2012) 334–341.

[46] W.J. Kim, D. Pradhan, B.K. Min, Y. Sohn, Adsorption/photocatalytic activity and fundamental natures of BiOCl and BiOCl<sub>x</sub>I<sub>1-x</sub> prepared in water and ethylene glycol environments, and Ag and Au-doping effects, *Appl. Catal. B: Environ.* 147 (2014) 711–725.

[47] H. Liu, Y. Su, Z. Chen, Z.T. Jin, Y. Wang, Graphene sheets grafted three-dimensional BiOBr<sub>0.7</sub>I<sub>0.3</sub> microspheres with excellent photocatalytic activity under visible light, *J. Hazard. Mater.* 266 (2014) 75–83.

[48] J. Di, J.X. Xia, M.X. Ji, B. Wang, S. Yin, Q. Zhang, Z.G. Chen, H.M. Li, Carbon quantum dots modified BiOCl ultrathin nanosheets with enhanced molecular oxygen activation ability for broad spectrum photocatalytic properties and mechanism insight, *ACS Appl. Mater. Interfaces* 7 (2015) 20111–20123.

[49] X. Zhang, L.Z. Zhang, Electronic and band structure tuning of ternary semiconductor photocatalysts by self doping: the case of BiO<sub>x</sub>, *J. Phys. Chem. C* 114 (2010) 18198–18206.

[50] Z.K. Xu, L. Han, B.H. Lou, X.W. Zhang, S.J. Dong, BiOBr<sub>x</sub>I(Cl)<sub>1-x</sub> based spectral tunable photodetectors fabricated by a facile interfacial self-assembly strategy, *J. Mater. Chem. C* 14 (2014) 2470–2474.

[51] G.G. Liu, T. Wang, S.X. Ouyang, L.Q. Liu, H.Y. Jiang, Q. Yu, T. Kako, J.H. Ye, Band-structure-controlled BiO(ClBr)<sub>(1-x)/2</sub>I<sub>x</sub> solid solutions for visible-light photocatalysis, *J. Mater. Chem. A* 3 (2015) 8123–8132.

[52] X. Xiao, R. Hao, M. Liang, X.X. Zuo, J.M. Nan, L.S. Li, W.D. Zhang, One-pot solvothermal synthesis of three-dimensional (3D) BiO<sub>x</sub>/BiOCl composites with enhanced visible-light photocatalytic activities for the degradation of bisphenol-A, *J. Hazard. Mater.* 233–234 (233) (2012) 122–130.

[53] D.S. Kong, The influence of fluoride on the physicochemical properties of anodic oxide films formed on titanium surfaces, *Langmuir* 24 (2008) 5324–5331.

[54] S.X. Weng, B.B. Chen, L.Y. Xie, Z.Y. Zheng, P. Liu, Facile in situ synthesis of a Bi/BiOCl nanocomposite with high photocatalytic activity, *J. Hazard. Mater.* 1 (2013) 3068–3075.

[55] X. Zhang, L.Z. Zhang, T.F. Xie, D.J. Wang, Low-temperature synthesis and high visible-light-induced photocatalytic activity of BiO<sub>x</sub>/TiO<sub>2</sub> heterostructures, *J. Phys. Chem. C* 113 (2009) 7371–7378.

[56] F.T. Li, Y. Zhao, Y.J. Hao, X.J. Wang, R.H. Liu, D.S. Zhao, D.M. Chen, N-doped P25 TiO<sub>2</sub>-amorphous Al<sub>2</sub>O<sub>3</sub> composites: one-step solution combustion preparation and enhanced visible-light photocatalytic activity, *J. Hazard. Mater.* 239–240 (2012) 118–127.

[57] F.T. Li, X.J. Wang, Y. Zhao, J.X. Liu, Y.J. Hao, R.H. Liu, D.S. Zhao, Ionic-liquid-assisted synthesis of high-visible-light-activated N-B-F-tri-doped mesoporous TiO<sub>2</sub> via a microwave route, *Appl. Catal. B: Environ.* 144 (2014) 442–453.

[58] F.T. Li, Q. Wang, X.J. Wang, B. Li, Y.J. Hao, R.H. Liu, D.S. Zhao, In-situ one-step synthesis of novel BiOCl/Bi<sub>24</sub>O<sub>31</sub>Cl<sub>10</sub> heterojunctions via self-combustion of ionic liquid with enhanced visible-light photocatalytic activities, *Appl. Catal. B: Environ.* 150 (2014) 574–584.

[59] F.T. Li, Q. Wang, J.R. Ran, Y.J. Hao, X.J. Wang, D.S. Zhao, S.Z. Qiao, Ionic liquid self-combustion synthesis of BiOBr/Bi<sub>24</sub>O<sub>31</sub>Br<sub>10</sub> heterojunctions with exceptional visible-light photocatalytic performances, *Nanoscale* 7 (2015) 1116–1126.

[60] H.W. Huang, X. Han, X.W. Li, S.C. Wang, P.K. Chu, Y.H. Zhang, Fabrication of multiple heterojunctions with tunable visible-light-active photocatalytic reactivity in BiOBr/BiO<sub>x</sub> full-range composites based on microstructure modulation and band structures, *ACS Appl. Mater. Interfaces* 7 (2015) 482–492.

[61] L. Suárez, H.Y. Dong, C. Pulgarín, R. Sanjines, Z.M. Qiang, J. Kiwi, Innovative photo-fenton catalysis by PE-FeO<sub>x</sub> films leading to methylene blue (MB) degradation: kinetics, surface properties and mechanism, *Appl. Catal. A: Gen.* 519 (2016) 68–77.

[62] H.G. Kim, P.H. Borse, W.Y. Choi, J.S. Lee, Photocatalytic nanodiodes for visible-Light photocatalysis, *Angew. Chem. Int. Ed.* 44 (2005) 4585–4589.

[63] X. Zhang, L.Z. Zhang, T.F. Xie, D.J. Wang, Low-temperature synthesis and high visible-light-induced photocatalytic activity of BiO<sub>x</sub>/TiO<sub>2</sub> heterostructures, *J. Phys. Chem. C* 113 (2009) 7371–7378.

[64] J. Kim, C.W. Lee, W. Choi, Platinized WO<sub>3</sub> as an environmental photocatalyst that generates OH radicals under visible light, *Environ. Sci. Technol.* 44 (2010) 6849–6854.

[65] D.T. Sawyer, J.S. Valentine, How super is superoxide? *Acc. Chem. Res.* 14 (1981) 393–400.

[66] G.T. Li, K.H. Wong, X.W. Zhang, C. Hu, J.C. Yu, R.C.Y. Chan, P.K. Wong, Degradation of acid orange 7 using magnetic AgBr under visible light: the roles of oxidizing species, *Chemosphere* 76 (2009) 1185–1191.